Title	Nondestructive characterization of laser powder bed fusion parts with neutron Bragg edge imaging
Author(s)	Busi M., Kalentics N., Morgano M., Griffiths S., Tremsin A. S., Shinohara Takenao, Loge R., Leinenbach C., Strobl M.
Citation	Additive Manufacturing, 39, p.101848_1-101848_9
Text Version	Published Journal Article
URL	https://jopss.jaea.go.jp/search/servlet/search?5075475
DOI	https://doi.org/10.1016/j.addma.2021.101848
Right	© 2021 The Author(s). Published by Elsevier B.V. This is an open access article under the CC BY-NC-ND license

Additive Manufacturing 39 (2021) 101848

Contents lists available at ScienceDirect

Additive Manufacturing

journal homepage: www.elsevier.com/locate/addma

Research paper

Nondestructive characterization of laser powder bed fusion parts with neutron Bragg edge imaging

Matteo Busi [a], Nikola Kalentics [b], Manuel Morgano [a], Seth Griffiths [c], Anton S. Tremsin [d], Takenao Shinohara [e], Roland Logé [b], Christian Leinenbach [c], Markus Strobl [a,*]

[a] Paul Scherrer Institute, Laboratory for Neutron Scattering and Imaging, 5232 Villigen, Forschungsstrasse 111, Switzerland
[b] Thermomechanical Metallurgy Laboratory - PX Group Chair, Ecole Polytechnique Fédérale de Lausanne (EPFL), CH-2002 Neuchâtel, Switzerland
[c] Empa-Swiss Federal Laboratories for Materials Science and Technology, CH-8600 Dübendorf, Switzerland
[d] University of California, Berkeley, CA 94720, USA
[e] J-PARC Center, Japan Atomic Energy Agency, Tokai, Ibaraki 319-1195, Japan

ARTICLE INFO

Keywords:
Additive manufacturing
Laser powder bed fusion
Selective laser melting
Neutron Bragg edge imaging
Strain mapping

ABSTRACT

Laser powder bed fusion is an efficient technique for additive manufacturing of metallic materials. The quality of the material produced depends on the optimization of a large range of build parameters and the complex thermo-mechanical build process is prone to inducing detrimental material features such as porosity and residual stresses negatively affecting fatigue resistance and lifetime. Here we apply neutron Bragg edge radiography in a parametric study on printing 316L steel. The parameters concerned are the laser scanning speed and strategy as well as the optional use of support structures. Analyses of the full field single shot wavelength-resolved Bragg edge radiography data enables to characterize local density inhomogeneities, as well as cracks, based on the long wavelength tail of the spectrum and variations of the stress field but also textural features based on the Bragg edge pattern. It is found that in the performed study not only respective differences in the residual stresses due to parameter variation are manifesting but also systematic irregularities due to machine imperfections (e.g. issues with the powder coater) are observed in the printed samples. The study supports the use of the parallel scanning strategy without supports and with the lower utilized scanning speed.

1. Introduction

In the last few decades, additive manufacturing (AM) has seen a rapid growth towards being one of the main technologies for the production of parts, in particular in the metal industry [1]. While developing towards enabling enhanced mechanical properties of the manufactured samples, AM allows for the production of highly individual and complex components [2], which are of particular interest in many fields such as implants for medical applications [3–5], but also aerospace [6], turbines [7] and robotics [8]. Among the specific AM techniques for metallic component production, one of the most promising and wide spread is laser powder bed fusion (LPBF) [9]. LPBF, also known as selective laser melting (SLM), is a method that produces metal components from metallic powders, using a high-intensity laser that repeatedly melts selective areas of powder, layer by layer, according to predefined digital models of the final part. Some of the drawbacks of LPBF are induced porosities, warping, cracking and detrimental tensile residual stresses (TRS), which are caused by the shrinkage during the liquid/solid, but also solid/solid phase transition [10,11]. The caused distortions or delaminations can in some cases even lead to failure during the build process.

The characterization of the material properties depending on the processing parameters plays a key role in the effort of reaching high standards of reliability and repeatability of the production chain concerning final product quality. Standard laboratory testing can access mechanical properties of the built materials, however, conventional techniques for the analysis of microstructures and residual stresses (e.g. hole drilling method [12], sectioning or contouring [13], and crack compliance or slitting [14]) are destructive, local and slow. Nondestructive testing using X-rays is often limited to surface analyses since, due to the high attenuation properties of many metallic materials, most of the signal is lost within the several millimeters or less. On the other hand, imaging and diffraction methods with neutron beams allow investigating the bulk of metallic components due to the high

* Corresponding author.
E-mail address: markus.strobl@psi.ch (M. Strobl).

https://doi.org/10.1016/j.addma.2021.101848

Available online 28 January 2021

penetration depths of neutrons in many relevant materials. In particular novel neutron imaging modalities based on diffraction contrast [15] enable assessments of large volumes through spatially resolved single exposure measurements returning information of local density, strains [15,16], phase composition [15,17] and texture variations [18,19]. The corresponding wavelength dispersive imaging is referred to as Bragg edge neutron imaging and can be exploited in 2D, in the form of projection imaging [15–17], or 3D in the form of tomography [15,20,21] and time resolved studies [22]. We have recently demonstrated that Bragg edge imaging can be applied efficiently to assess the residual stress induced in additively manufactured steel samples, in particular also in the surface regions and with spatial resolutions down to 55 μm, which enabled to study especially the effects of post processing treatments such as laser shock peening (LSP) [23].

Here we present a parametric study of LPBF of 316L austenitic stainless steel utilizing Bragg edge imaging with the aim of characterizing a number of features, namely density, stress and texture variations, simultaneously from a relatively large series of 48 samples, enabled by efficient single shot mapping. The variation of build parameters contained in the study concerned the laser scanning speed and strategy as well as the optional use of support structures. A systematic analysis of different features and regions of the attenuation coefficient spectrum including the Bragg edges enable the analyses of various material characteristics from single measurements. This study, with respect to the residual stresses analyses, supports the use of the parallel scanning strategy without support structures and utilizing the lower scanning speed, as the best results with respect to TRS at the surface and in depth are found for these settings. Moreover, we demonstrate the feasibility of simultaneous single shot multiple imaging modalities and their complementarity in the analysis of the results.

2. Materials and methods

2.1. Materials examined

The samples studied in this work are rectangular cuboids of 316L austenitic stainless steel (i.e. *Fe*-17*Cr*-12*Ni*). The samples were manufactured using MetcoAdd 316L powder (Oerlikon Metco, Switzerland; see supplement for material composition) and a Concept M2 machine (Concept Laser GmbH, Germany) equipped with a fiber laser operating in continuous mode with a Gaussian intensity distribution. The laser has a wavelength of 1070 nm and a spot size ($1/e^2$) of 90 μm. We produced several samples combining different build parameters and conditions. The laser scanning speed was set to *low*- and *high*-speed corresponding to 300 and 500 mm/s, respectively. Likewise, the samples were built *with* or *without* 3 mm thick support structures (see supplement for details). In both cases, the samples were cut via electro-discharge machining (EDM) in order to have the same sample height, where in the first case the support structure was cut and in the second case additionally printed bottom layers of the same material exceeding the target sample height were cut. Finally, the laser scanning strategy was modified. In the *parallel* mode, the powder layers are melted without a change in the scanning orientation within the same layer, but alternating laser directions rotated by 90 degrees at each layer. In the *chess* method, two orthogonal scanning orientations are alternated in a chessboard pattern with patches of size 5 × 5 mm within the same layer. The identical chessboard pattern is repeated for each layer. Other processing parameters such as laser power, hatch distance and powder layer thickness were kept fixed to 125 W, 105 μm and 30 μm, respectively. Table 1 details the sample labels and their respective combination of LPBF processing parameters. For each of the sample series listed in the table, we measured 6 individual specimens resulting in a total of 48 measured samples. The samples were produced under N_2 atmosphere and the O_2 content was kept below 1% during the process. The geometry of each resulting specimen was of approximately 12 × 14 mm^2 with building height of approximately 10 mm.

2.2. Measurements and instrumentation

The samples were measured at the time-of-flight (TOF) neutron imaging instrument RADEN [24] at the pulsed spallation neutron source of J-PARC, Japan. The neutron wavelengths used in these experiments range from 1.5 Å to 5.3 Å with a TOF wavelength resolution of approximately $\Delta\lambda/\lambda = 0.2\%$. Thus, the instrument is well suited to analyze the most pronounced Bragg edges of austenitic steel with resolutions suitable for strain mapping [15,16]. The detector used was a Micro-Channel Plate (MCP)/Timepix [25] detector suitable for TOF imaging applications. The current version of the detector still requires readout gaps in the data acquisition causing limited, tunable discontinuities in the detected TOF spectra. A standard correction algorithm is applied in order to correct for dead-time losses [26]. The detector features 512 × 512 pixels, with a pixel pitch of 55 μm for an overall field of view of 28.16 × 28.16 mm^2. This imaging setup enabled to image six samples simultaneously for each acquisition. The samples were grouped such that 6 samples of identical processing parameters were recorded in each of 8 corresponding exposures, resulting in a total of 48 samples measured. The exposure time for each set, i.e. also for each sample, was 4 h and the total measurement time for the full series of all 48 samples was 32 h.

2.3. Characterization method

Neutron Bragg edge imaging, used to measure the samples in this work, provides TOF spectra for all pixels of the 2D imaging detector by recording a TOF image series for each exposure of a sample set, i.e. wavelength increments of 0.001 Å. The datasets were rebinned combining every consecutive 4 TOF bins, resulting in wavelength increments of 0.004 Å, to increase neutron statistics and improve the log-normalization into attenuation coefficient through Beer-Lambert's law, and to approach the instrument resolution of 0.02% in the considered wavelength bandwidth. The additional dimension in the image data given by the time-of-flight of neutrons enables multiple contrast and thus analyses modalities to be exploited. In contrast to conventional neutron imaging, which typically offers only a wavelength averaged attenuation contrast image to assess macroscopic structural features, the analyses of different spectral features contain significantly more information.

Fig. 1 displays the example of two TOF spectra extracted from a sample of the set A and E, respectively, and a theoretical reference spectrum calculated with the NXS plotter [27]. The discrepancies between the measured and nominal reference spectra are due to primary extinction caused by the finite crystallite size of the sample and texture properties of the material, which are not included in the reference calculation. The Figure illustrates not only significant spectral differences for the respective samples but also, schematically, which different parts and features of the spectra are used in this work to analyze

Table 1
List of the sample labels and their respective combination of the LPBF processing parameters.

Sample series	A	B	C	D	E	F	G	H
Laser speed	High	High	High	High	Low	Low	Low	Low
Strategy	Parallel	Parallel	Chess	Chess	Parallel	Parallel	Chess	Chess
Support structure	×	✓	×	✓	×	✓	×	✓

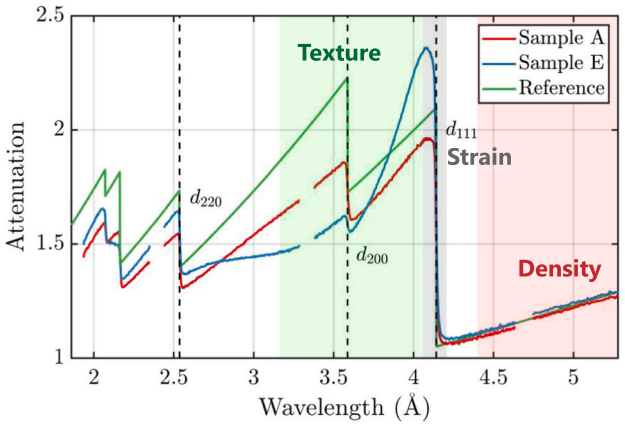

Fig. 1. Neutron Bragg edge transmission spectra exemplified for an individual specimen of the A and E sample series and a reference spectrum of untextured 316L stainless steel calculated with the NXS plotter [27]. The cuts in the measured spectra are due to the required detector readout gaps. The Bragg edges corresponding to the lattice planes (111), (200) and (220) are indicated. The wavelength resolution of the technique allows multiple imaging modalities. Relative changes in the Bragg edges and the shape of the spectra reveal texture effects in the samples. The tracking of the position of a specific Bragg edge can be used to calculate the strain of the corresponding lattice planes. The linear part of the spectrum is suitable to reveal the bulk density of the materials.

different properties of the investigated materials. The first and most straightforward imaging mode is mapping the attenuation coefficient, providing a density map and an image of macroscopic structural features such as pores and cracks. However, in conventional imaging, utilizing a broad spectrum, the fact that the attenuation coefficient is the sum of scattering and absorption contributions can induce biases due to anisotropic scattering characteristics. Thus, a density map is best achieved by only utilizing the spectral part beyond the last Bragg edge, where the signal is only due to absorption. Therefore integrating the signal over all wavelengths beyond the last Bragg edge of austenitic steel, i.e. the (111) Bragg edge at about 4.1 Å, yields reliable density maps of the investigated samples of constant thickness. The density, ρ, was calculated from the measured attenuation coefficient, $\mu(\lambda)$, using the relation:

$$\rho = \rho_{ref} \frac{\int_{\lambda_{abs}} \mu(\lambda) d\lambda}{\int_{\lambda_{abs}} \mu_{ref}(\lambda) d\lambda}, \tag{1}$$

assuming fixed cross sections, and only a scaling impact from the density. Therein, $\rho_{ref} = 8.045$ g/cm^3 is the nominal density of the 316L stainless steel and $\mu_{ref}(\lambda)$ is its respective theoretical attenuation coefficient spectrum, calculated with NXS software [27]. λ_{abs}, is the wavelength bandwidth where the absorption cross section is dominating the attenuation coefficients which is between 4.2 Å and 5.3 Å.

On the other hand, texture variations, which could bias conventional attenuation contrast, can be mapped separately, e.g. by assessing the full Bragg edge spectra. However, given the large number of spectra and the fact that texture effects can be quite specific, a simple method aimed only at mapping variations of texture is to limit image contrast to integrals of specific regions between specific Bragg edges. For example, the differences of the spectra between sample A and E in Fig. 1 suggest that a different average texture is introduced in the samples by changing the scanning laser speed from 500 mm/s to 300 mm/s, as reported in previous studies [28,29]. Finally, tracking of the Bragg edge positions with high resolution provides access to local residual strains corresponding to specific lattice planes. The measured strains are in neutron beam direction and like all other parameters averaged over the sample thickness.

For a specific crystal lattice family *hkl*, with lattice spacing d_{hkl}, the scattering angle increases according to Bragg's law with the wavelength (λ) up to $\lambda = 2d_{hkl}\sin(\pi/2)$. Beyond this wavelength, the Bragg condition cannot be satisfied any longer, which results in a sharp drop of the material's attenuation coefficient, the so-called Bragg edge. Therefore, changes in the wavelength at which the Bragg edge occurs corresponds to changes in the interplanar lattice spacing d_{hkl}. These can in turn be used to calculate the elastic lattice strain, ϵ_{hkl}, of a material according to the equation:

$$\epsilon_{hkl} = \frac{d_{hkl} - d^0_{hkl}}{d^0_{hkl}}, \tag{2}$$

where d^0_{hkl} represents the unstrained lattice parameter reference. Different methods, often the measurement of an unstrained annealed reference sample, are utilized to evaluate d^0_{hkl}. The residual lattice stress, σ_{hkl} (MPa), can then be calculated when assuming linear elasticity, and a specific Young's modulus, E, using the equation:

$$E = \sigma_{hkl}/\epsilon_{hkl}. \tag{3}$$

In this work, the considered lattice plane is the (111) and the Young's modulus assumed for the material is 261 GPa according to literature [30]. Despite the (311) plane being in general most suited for residual stresses determination due to being insensible to intergranular strains [31], we used the (111) due to a significantly stronger signal for this edge, providing more reliable data.

In this work, the Bragg edge positions have been evaluated by a first order Gaussian fit of the derivative of the measured transmission spectrum in a wavelength bandwidth containing the Bragg edge at approximately 4.1 Å. The center of the Gaussian fit corresponds to the Bragg edge position λ_{111} and, hence, with $d_{111} = \lambda_{111}/2$ to the lattice parameter. To improve the neutron statistics, prior to the Gaussian fit, a moving average in the direction orthogonal to the build direction was applied, since the main part of analyses focuses on the build direction and the variation of strain in that direction. This was done by a convolution of the individual TOF-frames with a one directional Gaussian custom kernel. The reference lattice parameter d^0_{hkl} was extracted from samples that have been annealed after the AM build process. The annealing was carried out at 1100 °C for 10 min. This method was validated in a previous work [23] with the hole drilling method (HDM) by comparing measures strains in the surface region of identical samples from both Bragg edge imaging and HDM. The results have shown good agreement, but also underlined the higher resolution of HDM at the surface and better accuracy of Bragg edge imaging beyond about 1 mm depth under the surface, where HDM becomes unreliable [32]. In the present work, we further convert the strain to residual stress using Eq. (3), and our results reported in the next sections are in agreement with the literature range of values for additively manufacturing stainless steels [33–35]. Together, these evaluation steps allowed producing residual stress maps (using Eq. (3)) and thus, to analyze the dependence of stress fields in the sample on the different LPBF processing parameters.

3. Results and discussion

Fig. 2 shows density maps according to the attenuation coefficient for wavelengths above 4.2 Å and stress maps with regards to the (111) lattice planes for a selection of samples, one of each considered combination of the LPBF processing parameter. Note that the specimens shown in the figure were selected from separate measurements to illustrate the key features observed. Every graph displays a curve showing the residual stress line profile versus build direction, averaged along the neutron beam direction and the sample width, for two respective samples displayed as well as for the corresponding average of all samples measured with the same processing parameters. While for the density maps derived from absorption, the focus is on the one hand on individual features like cracks, but also on the overall density and density homogeneity depending on the build parameters, for the stress

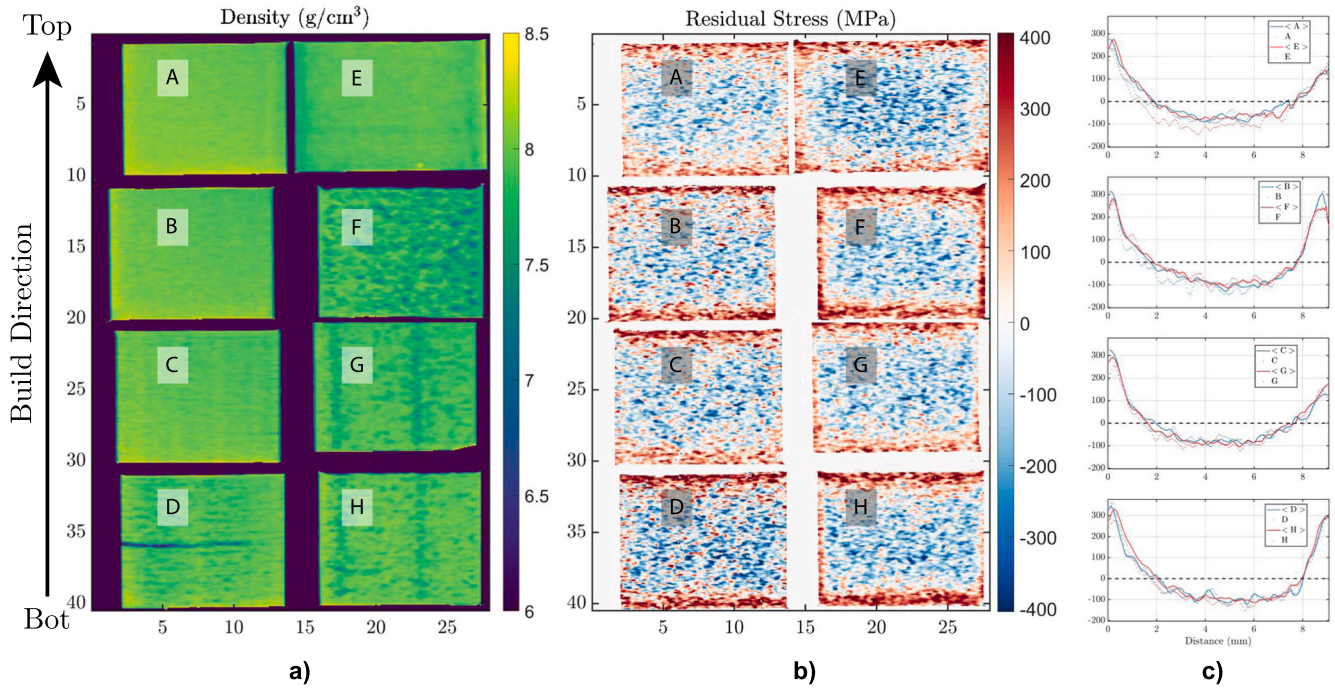

Fig. 2. Density (a) and residual stress (b) map and average residual stress along the build direction (c) of the samples measured. The labels corresponds to the different LPBF processing parameters detailed in Table 2. Note that the field of view does not correspond to the detector panel but is an assortment. The build direction from bottom (Bot) to the top (Top) corresponds to the direction in which the layers are additively printed. For the residual stress profiles, both the individual specimens shown in the maps (dots) and the average of all the samples from the same series (solid line) are represented.

maps mainly the averaged results with respect to specific AM parameters will be considered further on in order to investigate systematic effects.

3.1. Attenuation coefficient-based analysis

Fig. 2 shows the density maps of the samples derived for wavelengths for which basically only absorption contributes to the beam attenuation. For the constant thickness of the samples, as discussed above, the attenuation coefficient can be calculated from the signal and is linearly proportional to the material bulk density. Fig. 3 shows in turns the average density and relative standard deviation of each sample series as well as the individual average density of each specimen. While the corresponding images provide spatial information on the density variations and thus also macroscopic production faults, the chart provides

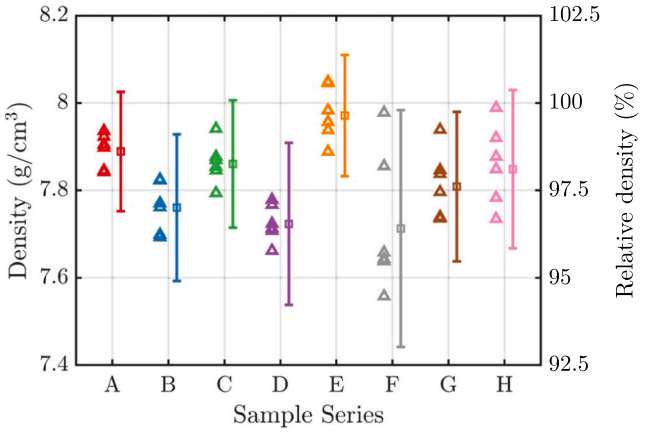

Fig. 3. Average density of each specimen for each sample series (triangle) and the average density of each sample series (squares). The relative density axis on the right is the relative deviation (%) from the nominal density of 8 g/cm³. The error-bars respective to the latter corresponds to the standard deviation.

quantitative comparisons of the average sample densities resulting from different processing parameters. It is observed that the samples built with high laser scanning speed (A–D) have overall a homogeneous internal density distribution, which was found for all the samples measured. However the samples built with support structures (B, D) result in a decreased average density. Furthermore, for one sample of the B and D series, which are both built with the aid of support structures (compare Table 2), a delamination such as the one shown for sample D in Fig. 2 was observed. This is assumed to be caused by the accumulation of excessive TRS in the respective printed layers, which can indeed result in delamination processes. Despite the significant signature in the absorption signal (app. −15%) in the delaminated region, no impact on the resulting residual stress in this region could be found. However, this region is, after conclusion of the build process, under compressive stresses and thus a premature release of TRS in this region during the build process through delamination would have lost significance.

Most of the samples built with low laser scanning speed (E–H), except for the sample series E and a few individuals for each sample series, exhibit in contrast a more inhomogeneous density distribution that results in a decreased average density. The lower density indicates higher porosity, which, however, also appears inhomogeneously distributed throughout the samples. In the corresponding samples displayed in Fig. 2 an irregular variation is observed e.g. for the sample of the series F, while distinct patterns are recognized for the samples of series G and H (but also D, from the higher laser speed series). The higher porosity can be attributed to the laser scanning speed that in these cases is lower than the considered optimal value. Excessively high scanning speeds would also lead to porosity, in this case lack of fusion pores. It is in fact found, that samples produced with the lower scanning speed value and which did not show effects of inhomogeneous density distributions, had overall a higher density than the ones built with the higher speed.

The regular density feature visible for samples G and H (both built with chess strategy and lower scanning speed) in Fig. 2 are vertical strips, along the build direction, of lower density. Despite several of the

Table 2
List of all the types of samples scanned with different LPBF additive manufacturing parameters and their labels. The key material parameters summarized are extrapolated from Fig. 2. The surface TRS (i.e. at the depth of 55 μm) and the depth at which it converts to compressive residual stress are listed. Note that the pixel size of the detector is 55 μm thus, the surface TRS reflects the average value within the first 55 μm. It also details the maximum TRS value and its respective depth from the sample surface. For each of these parameters, the respective standard deviation, σ, is reported as well.

Sample series	A	B	C	D	E	F	G	H
Surface TRS (MPa)	275.3	309.8	324.9	329.9	230.6	237.5	269.2	275.7
σ	64.4	40.2	23.1	31.0	55.2	57.6	82.9	49.9
TRS depth (mm)	1.92	1.76	1.98	2.09	1.87	1.87	1.65	2.01
σ	0.26	0.30	0.51	0.35	0.74	0.15	0.32	0.19
Max TRS (MPa)	275.3	313.1	324.9	347.2	274.3	290.9	283.0	328.5
σ	69.8	20.7	25.0	24.8	35.5	42.7	48.7	60.1
Max TRS depth (mm)	0.05	0.11	0.05	0.11	0.22	0.22	0.22	0.27
σ	0.05	0.05	0.03	0.03	0.03	0.07	0.12	0.11

samples belonging to these series showing this effect, it does not seem to be correlated specifically with the LPBF processing parameters, but rather with the position on the build plate during production. Thus, it is assumed that these traits were rather caused by scratches of the coating blade of the powder coater, which cause an uneven powder bed deposition and consequently lower local material densities. Overall, considering all samples and build conditions of the samples in this work, the best densities with consistency and repeatability were found for the lower scanning speed of 300 mm/s with parallel strategy and without using support structures. The higher speed of 500 mm/s gave relatively high densities with consistency and repeatability for both parallel and chess strategy, but without using a support structure.

3.2. Residual stress analysis

Fig. 2 also shows the maps of the residual stress distribution in selected samples. All samples showed a significant rise of TRS in the proximity of the surfaces of the samples, especially at the two extremes of the build direction, whereas only in some cases (e.g. samples F, H) it is also strong towards the vertical sides. The central part of the samples in turn display a flat region of negative values of residual stress, i.e. compressive residual stress (CRS). In the remainder of this section, the focus will be separately on the residual stress produced in the proximity of the different surfaces of the specimen that is crucial for the fatigue behavior of the material.

3.2.1. Top sample surface

Fig. 4 shows plots of residual stress as a function of the distance from the samples' top surface for the different LPBF processing parameters. These profiles along the build direction were obtained by averaging the profiles of all samples produced with the same LPBF processing parameters and displaying equivalent individual profiles. Only the first 3 mm are displayed. The key quantities to benchmark the profiles are illustrated in the graphs, exemplified for individual plots. The most relevant one is the TRS at approximately 55 μm (first spatial bin with the utilized spatial resolution) from the sample's surface that we refer to as surface TRS. It is particularly important for the fatigue and stress resistance of the material [36]. We also indicate the depth at which the tensile residual stress turns into CRS, which corresponds to the surface region with higher crack propagation rate and weakness to fatigue [33]. Finally, we report the maximum TRS value and its respective depth from the surface. Table 2 details all these features for each of the sample groups measured. The lines are grouped by samples built with the same laser scanning speed as these groups present similar TRS trends that are distinct only by a change in the other two parameters.

A notable difference between the two groups of plots in Fig. 4 is the different trend of TRS in the proximity of the top surface. While the maximum TRS of the samples built with higher speed (A, B, C, D) are occurring right at the surface or within 110 μm (two spatial bins), for the samples built with lower speed (E, F, G, H) the TRS rises from the surface to its maximum at a depth between 220 and 270 μm. In connection with this, it is observed that the surface TRS yields lower values for all samples manufactured with the lower laser scanning speed (E, F, G, H), compared to all higher laser speed counterparts (A, B, C, D). This is because a lower scanning speed setting yields faster cooling rates [37, 38] and the overall increase in the temperature of the sample is beneficial for the relief of stress [39]. However, the maximum value of TRS is lower for the samples built with higher scanning speed compared to the

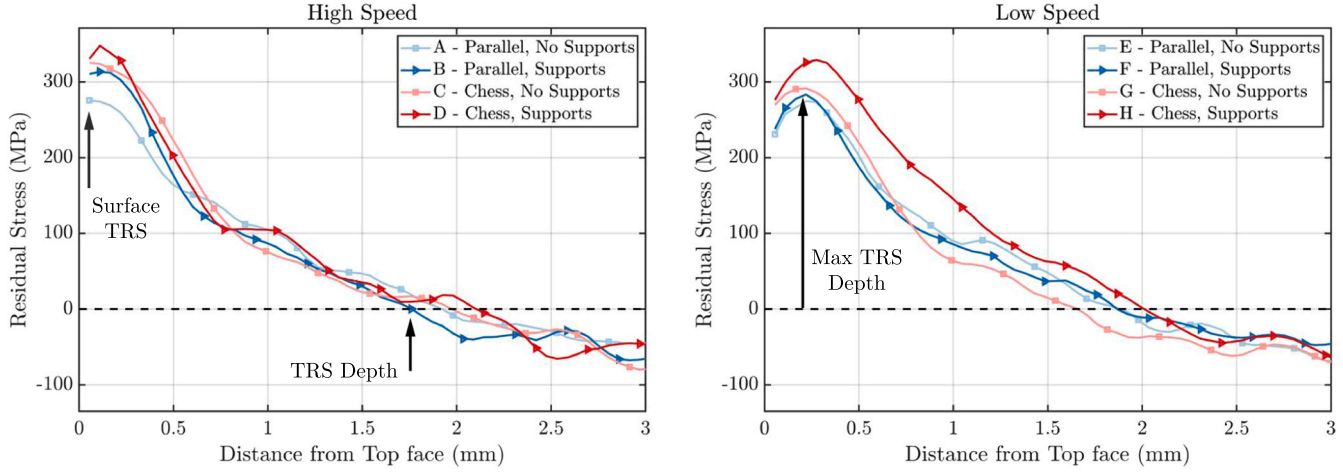

Fig. 4. Residual stress (MPa) along the depth (mm) from the surface of the face of the sample at the end of the build direction. The different samples are grouped as high (left) and low (right) laser speed. The color code is different for samples printed with parallel (blue) and chess (red) laser scanning strategy. The markers are respective to the samples build without (squares) and with (triangles) the aid of support structures.

lower speed counterparts, even though the latter are found deeper into the sample.

The depth of the TRS conversion to CRS are overall between the lower and upper limit of 1.6 mm and 2.1 mm, respectively. There does not seem to be a particular correlation with the LPBF processing parameters besides the fact that the samples built with chess scanning strategy and support structures both yield systematically deeper values for both laser speeds (D, H).

The chessboard strategy (C, D, G, H) does not appear to have improved TRS. On the contrary, we observed an increase in both surface and maximum TRS (see Table 2). Controversial results are reported in the literature with respect to the effect of the scanning strategy on the residual stress, due to the complexity and large number of degrees of freedom in the choice of the scanning paths and lengths [40]. Our findings support a recent study that shows that alternating the parallel scanning strategy at each layer by a rotation of 90 degrees achieves weaker residual stresses [40]. Similarly, the use of support structures (B, D, F, H) also led to higher values in both surface and maximum TRS. The difference in surface TRS is, however, of little significance. Furthermore, for the samples built with higher speed (A-D), the support structures (B, D) appear to induce a minor offset of about 60 μm in the maximum TRS depth, which for low laser speed (E-H) is similarly only found for the chess strategy (H).

3.2.2. Bottom sample surface

A similar analysis as the previous was performed for the bottom surfaces of the samples, which was expected to especially display the impact of the support structures. Fig. 5 and Table 3 show the corresponding profiles in this region equivalent to Fig. 5 dealing with the top surface. Overall, the same trends that were observed for the top faces of the samples are confirmed on this side, with, however, a stronger impact from the use of support structures.

First, looking into the TRS depth, it is observed that the samples built without supports structure (A, C, E, G) have deeper reaching TRS compared to their counterparts built with support structures (B, D, F, H). While the former values are confined between 1.27 mm and 1.35 mm, the latter spread between 1.57 mm and 1.82 mm. However, this comes with a significant, but opposed difference in both the surface and maximum TRS magnitudes. The samples built without support structures (A, C, E, G) have their maximum TRS located at the surface, whereas the ones built with support structures (B, D, F, H) display these at between 0.22 mm and 0.33 mm depth beneath the surface. Furthermore, the latter have significantly higher maximum and surface TRS compared to their counterparts without support structure. This means the stress profiles without support structures display a much flatter slope from surface towards the central compressive region. These results indicate that the EDM cutting that is performed on the samples built without support structures at a limited distance from the support plate, does not imply surface TRS at the bottom of the sample comparable to those of the bottom LPBF layers with limited interface to the specific support structure utilized for other samples. In addition, samples built with chess strategy have a tendency of higher maximum and surface TRS values and in general slightly higher TRS in the surface region, compared to the samples built with parallel strategy, but otherwise same parameters. However, the impact of the strategy seems to be of minor influence compared with the use of support structures.

3.2.3. Vertical sides

Finally, we studied the vertical sides of the samples, i.e. the sides parallel to the build direction. Fig. 6 shows the corresponding mean residual stress profiles as a function of the distance from both surfaces, i.e. either the left or right sample surface, grouped according to whether they were manufactured with or without support structures. It is observed that samples built with support structures (B, D, F, H) have systematically higher TRS than the 'no support' counterparts (A, C, E, G). Likewise, samples built with the low scanning speed (E, F, G, H) have systematically higher TRS than high-speed counterparts (A, B, C, D) with otherwise same build parameters. No noticeable systematic differences are found in this case between parallel and chess scanning strategies. However, the left and right side surface trends seem to match more consistently for samples built with parallel scanning strategy (A, B, E, F). We also observed that samples F (low laser speed, parallel scanning and supports) show a significantly higher amount of surface TRS. Samples F are also those with the most severe irregular inhomogeneities in density distribution.

3.3. Texture analysis

Texture affects the Bragg edge pattern of the wavelength dependent transmission in various forms, depending on the specific texture with respect to the transmission direction. In a first attempt to identify texture features in the samples, we inspected attenuation coefficient images for relatively narrow wavelength ranges near the Bragg edges corresponding to the (220), (200) and (111) lattice planes (2.5, 3.6 and 4.1 Å respectively). For an integrated bandwidth just below the (111) Bragg edge, the strongest contrast was identified for some repeatedly appearing features in some of the samples. Further inspection of the Bragg edge patterns of the appearing sample regions of interest (ROI) resulted in identifying the strongest variations in the height of the last and most distinct (111) Bragg edge, but also in particular the height of the (220)

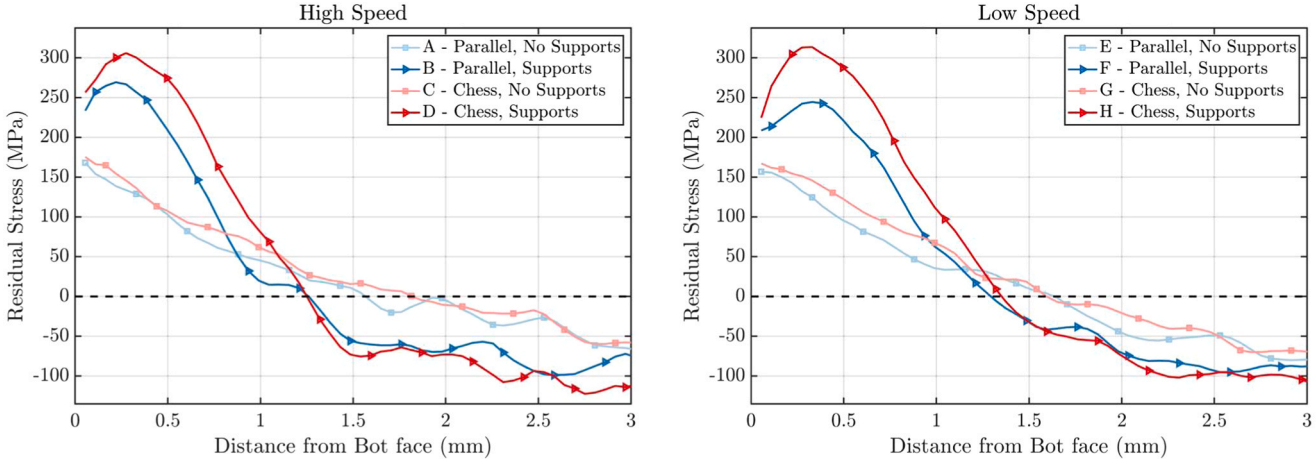

Fig. 5. Residual stress (MPa) along the depth (mm) from the surface of the face of the sample closest to the support structure, i.e. where the samples lay down. The grouping of the lines is done equivalently as in Fig. 4.

Table 3
Similarly as Table 2, this summarize the key material parameters respective to Fig. 5. For each of these parameters, the respective standard deviation, σ, is reported as well.

Label	A	B	C	D	E	F	G	H
Surface TRS (MPa)	167.8	233.1	175.2	256.1	156.6	208.3	166.9	224.1
σ	28.9	15.7	40.9	60.6	35.6	62.4	13.8	50.8
TRS depth (μm)	1.57	1.27	1.82	1.27	1.65	1.29	1.60	1.35
σ	0.35	0.17	0.19	0.12	0.25	0.13	0.29	0.09
Max TRS (MPa)	167.8	268.8	175.2	305.4	156.6	244.1	166.9	312.9
σ	25.11	21.2	33.7	42.1	25.2	24.6	11.6	25.9
Max TRS depth (mm)	0.05	0.22	0.05	0.27	0.05	0.33	0.05	0.33
σ	0.10	0.05	0.05	0.13	0.13	0.15	0.10	0.07

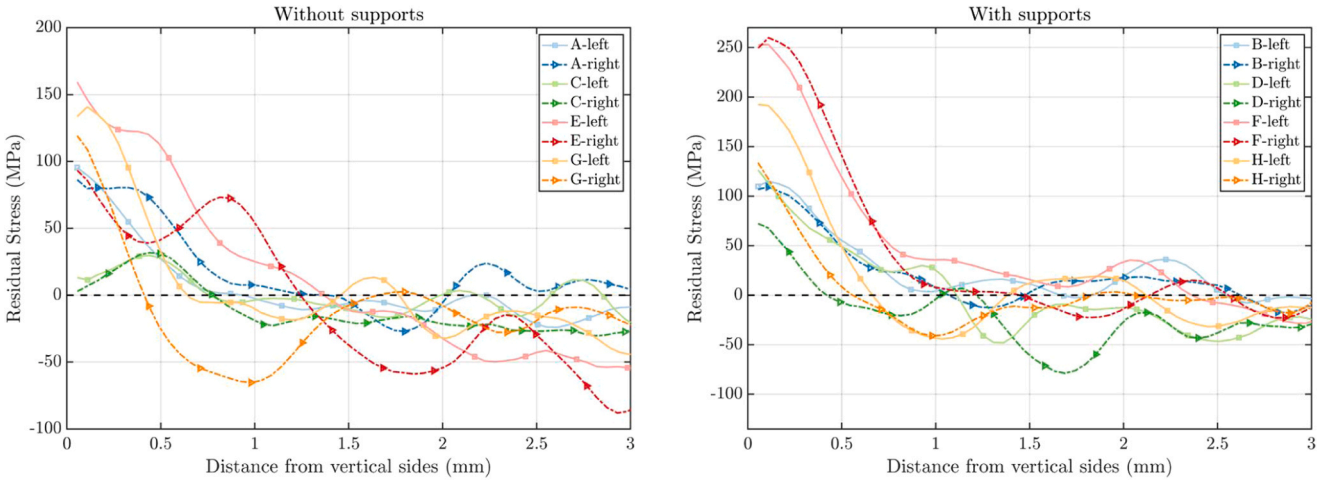

Fig. 6. Residual stress (MPa) as a function of distance from the vertical sides of the samples, grouped as the samples built without support structures (left) and with support structures (right). The dashed-dotted and solid lines corresponds right and left sides of the samples respectively. The color code is fixed for each LPBF parameter combination, while the opacity changes are to remark the different sample sides (left vs. right).

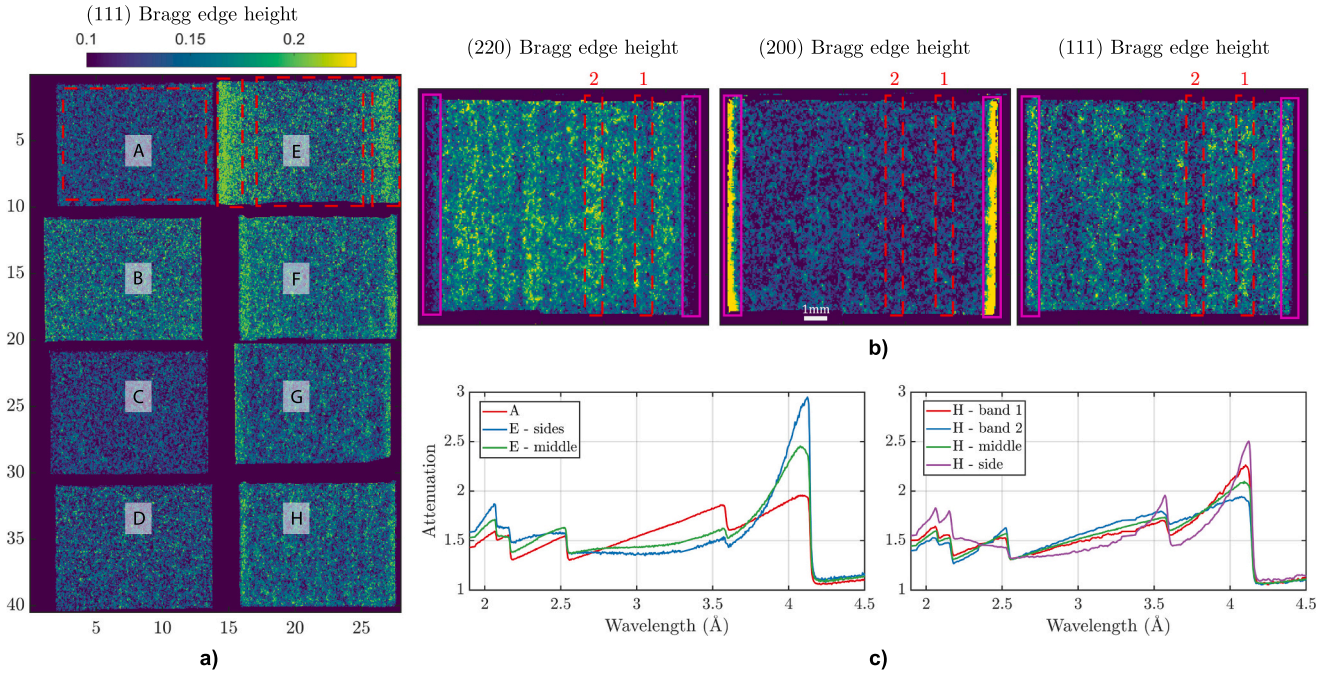

Fig. 7. (a) Maps of the (111) Bragg edge height respective to the sample maps in Fig. 2. The two dashed red boxes show the regions respective to the spectra of samples A and E plotted in (c). (b) Maps of the (220), (200) and (111) Bragg edge height respective to the sample shown for the series H. (c) Attenuation coefficient spectrum shown for the marked regions in (a) and (b) (compare with the legend in the graphs to identify the regions in the radiographs represented in the cross-section in (c)). Note that the color map in the graphs (a) and (b) are blue to yellow according to increasing Bragg edge height.

Bragg edge. Therefore, mapping the Bragg edge height from the same fitting procedure as applied for the strain maps was used to map texture homogeneity, respective to the variations of the samples. Fig. 7 displays the corresponding (111) Bragg edge height maps of the respective samples shown in Fig. 2. In addition, three close ups of the specimen from the sample series H are shown for the (220), (200) and (111) Brag edges. No texture variations within the image of any sample built with the higher scanning speed (A, B, C, D) could be identified and all samples measured in these groups displayed spectra comparable to the one represented for the full sample ROI of sample A in Fig. 7, which is close to that of an isotropic powder structure (compare Fig. 1). However, samples built with the lower scanning speed (E, F, G, H) all showed texture variations throughout the samples, which are also exemplified in Fig. 7. First, all samples from these series have shown a strong texture variation in the proximity of the vertical surfaces, similar to the one shown particularly prominent for the 3.6 Å Bragg edge (200) of the sample H. The TOF spectra for regions (Fig. 7c) at these sides display significantly sharper and greater Bragg edges heights corresponding to the (111) and (200) lattice planes with a steeper rise towards the maxima on the lower wavelength side. This appears to indicate a preferential orientation of these lattice planes perpendicular to the beam direction in these peripheral regions of the sample. This is because when the LPBF processing is carried out in low speed setting, when reaching the vertical sides of the samples, the laser speed is decreased even further, causing even stronger preferred orientation.

Another effect that was observed for all samples built with the lower scanning speed and parallel strategy (E, F) was a gradient in the maps from the center of the samples towards the vertical sides, which was confirmed by individual assessment of respective spectra. This could be caused by temperature gradients, which increase and become most anisotropic towards the edges, and thus might cause specific texture developing in such regions. Differently from this, for the samples produced with the lower scanning speed and chess strategy (G, H), we observed vertical stripe patterns (along the build direction) such as the ones in the marked regions of the sample from the H series in Fig. 7. We stress that (to the best of our knowledge) no other techniques allow identification of such microstructural gradients over length scales of mm in probed volumes on the order of a few centimeters. The corresponding variations of the TOF spectra confirm the presence of a varying crystallographic texture in the samples. We observe that the texture features found in the maps have vertical symmetry, predominantly at sample edges, indicating that they are caused by either specific settings of the LPBF scanning strategy or are related to issues with the coating blade of the powder coater, as discussed in the previous section. Furthermore, Fig. 7c shows in the left panel the Bragg pattern spectrum integrated for large volumes of the samples, exemplifying the typical overall sample spectra difference between changing the LPBF processing speed from high (sample A) to low (sample E). We find that integrating the TOF spectrum in the whole sample volume, the samples built with low speed (E–H) display stronger texture effects such as greater (111) Bragg edge heights and smaller (200) Bragg edge heights, indicating stronger preferential crystallographic orientation of these lattice planes. Also in the surface regions of the side faces of this sample, where the laser speed falls to even lower values and temperature gradients are most pronounced, the texture deviations in Bragg edge height and shape are clearly more marked. The dependence of the crystallographic texture on the LPBF scanning speed was indeed observed in previous studies, performed with neutron diffraction and electron back scattering diffraction (EBSD). For example Leicht et al. showed that in wide and shallow melt pools (which are obtained with high speed) grains solidify preferably in the <001> direction along the build direction, whereas in narrow and deep melt pools (low speed) a <101> texture (diagonal) is usually observed [28,29]. However, a deeper quantitative analysis of the texture and preferred lattice orientations is beyond the scope of this study, and is planned for future investigation and analyses.

4. Conclusions

Bragg edge imaging has been applied to study variations of density, residual stress and texture in an extensive sample series of as-built specimens produced by LPBF additive manufacturing. The simultaneous characterization of these multiple properties is unique to this technique to the best of our knowledge. Samples were built by systematic variation of three build parameters, namely laser scanning speed, scanning strategy and supports. The comparative study on the one hand demonstrates the capabilities of Bragg edge neutron imaging for efficient single shot full field assessment of multiple material characteristics ranging from density via stress maps to texture variations, enabling the study of large sample series. On the other hand, the results of the study revealed several individual build failures involving cracks, but also alterations in density due to machine issues, and systematic features and differences due to the variation of the build parameters. Variations in density could be related to the applied laser speed, with the conclusion that the lower speed was more prone to produce artefacts and density variations, but also has the potential to produce the highest densities. Some density variations, however, are assumed to be related to machine issues. For the higher laser scanning speed, the support structures had a negative impact on the densities achieved. Overall, no better performance was found for employing the chess scanning strategy, compared to the parallel strategy. In most cases, the latter resulted in lower TRS at the sample surfaces. Likewise, LPBF processing of samples without the aid of support structures resulted in lower surface TRS for all measured samples. Samples exhibiting the lowest values of TRS were found in the E series, which means for parallel scan strategy, no supports and the lower speed. This series also exhibited the highest densities. However, all samples processed with the lower speed could be shown to display inhomogeneous texture, which in some cases might be related to the density variations induced by the damaged coater, but affected in particular the side surfaces of the samples.

CRediT authorship contribution statement

Matteo Busi: Software, Methodology, Validation, Formal analysis, Data curation, Writing - original draft, Writing - review & editing, Visualization. **Nikola Kalentics:** Validation, Investigation, Resources, Writing - review & editing. **Manuel Morgano:** Investigation, Writing - review & editing. **Seth Griffiths:** Resources, Writing - review & editing. **Anton S. Tremsin:** Resources, Writing - review & editing. **Takenao Shinohara:** Resources, Writing - review &editing. **Christian Leinenbach:** Resources, Methodology, Funding acquisition, Writing - review & editing. **Roland Loge:** Resources, Methodology, Supervision, Funding acquisition, Writing - review & editing. **Markus Strobl:** Conceptualization, Methodology, Investigation, Resources, Writing - original draft, Writing - review & editing, Supervision, Project administration, Funding acquisition.

Declaration of Competing Interest

The authors declare that they have no known competing financial interests or personal relationships that could have appeared to influence the work reported in this paper.

Acknowledgements

The project was enabled partially through funding from the Strategic Focus Area Advanced Manufacturing (SFA-AM), an initiative of the ETH Board. M.B. acknowledges funding from DanScatt. NK and RL gratefully acknowledge the generous support of PX Group to the LMTM laboratory. MS expresses acknowledgment for the awarded beamtime at JPARC under the proposal number 2019A0215.

Appendix A. Supporting information

Supplementary data associated with this article can be found in the online version at doi:10.1016/j.addma.2021.101848.

References

[1] D. Herzog, V. Seyda, E. Wycisk, C. Emmelmann, Additive manufacturing of metals, Acta Mater. 117 (2016) 371–392.
[2] N. Guo, M.C. Leu, Additive manufacturing: technology, applications and research needs, Front. Mech. Eng. 8 (2013) 215–243.
[3] D. Bourell, et al., Microscale metal additive manufacturing of multi-component medical devices, Rapid Prototyp. J. (2010).
[4] J.-P., Kruth, B., Vandenbroucke, J., Van Vaerenbergh, I., Naert, Rapid manufacturing of dental prostheses by means of selective laser sintering/melting, in: Proceedings of the AFPR S 4, 2005, 176–186.
[5] X.-b. Su, Y.-q. YANG, Y. Peng, J.-f. SUN, Development of porous medical implant scaffolds via laser additive manufacturing, Trans. Nonferrous Met. Soc. China 22 (2012) s181–s187.
[6] D., Türk, et al. Additive manufacturing with composites for integrated aircraft structures, in: Proceedings of the International SAMPE Technical Conference, 1404–1418 (Society for the Advancement of Material and Process Engineering, 2016.
[7] L.N. Carter, M.M. Attallah, R.C. Reed, Laser powder bed fabrication of nickel-base superalloys: influence of parameters; characterisation, quantification and mitigation of cracking, Superalloys 2012 (2012) 577–586.
[8] C., Semini, et al. Additive manufacturing for agile legged robots with hydraulic actuation, in: Proceedings of the 2015 International Conference on Advanced Robotics (ICAR), 123–129 (IEEE, 2015).
[9] C.Y. Yap, et al., Review of selective laser melting: materials and applications, Appl. Phys. Rev. 2 (2015), 041101.
[10] J. Oliveira, T. Santos, R. Miranda, Revisiting fundamental welding concepts to improve additive manufacturing: from theory to practice, Prog. Mater. Sci. 107 (2020), 100590.
[11] J.P. Oliveira, A. LaLonde, J. Ma, Processing parameters in laser powder bed fusion metal additive manufacturing, Mater. Des. 193 (2020), 108762.
[12] Standard test method for determining residual stresses by the hole-drilling strain-gage method, in: Proceedings of the ASTM, E, 837–95, 2008.
[13] M.B. Prime, Cross-sectional mapping of residual stresses by measuring the surface contour after a cut, J. Eng. Mater. Technol. 123 (2001) 162–168.
[14] M.B. Prime, Residual stress measurement by successive extension of a slot: the crack compliance method, Appl. Mech. Rev. (1999).
[15] R. Woracek, J. Santisteban, A. Fedrigo, M. Strobl, Diffraction in neutron imaging—a review, Nucl. Instrum. Methods Phys. Res. Sect. A Accel. Spectrom. Detect. Assoc. Equip. 878 (2018) 141–158.
[16] J.R. Santisteban, A. Steuwer, L. Edwards, P. Withers, M. Fitzpatrick, Mapping of unstressed lattice parameters using pulsed neutron transmission diffraction, J. Appl. Crystallogr. 35 (2002) 497–504.
[17] A. Steuwer, P. Withers, J. Santisteban, L. Edwards, Using pulsed neutron transmission for crystalline phase imaging and analysis, J. Appl. Phys. 97 (2005), 074903.
[18] T. Watkins, et al., Neutron characterization for additive manufacturing, Adv. Mater. Process. 117 (2013) 23–27.
[19] J. Santisteban, et al., Texture imaging of zirconium based components by total neutron cross-section experiments, J. Nucl. Mater. 425 (2012) 218–227.
[20] C.M. Wensrich, et al., Bragg-edge neutron transmission strain tomography for in situ loadings, Nucl. Instrum. Methods Phys. Res. Sect. B Beam Interact. Mater. Atoms 383 (2016) 52–58.
[21] R. Woracek, et al., Neutron Bragg edge tomography for phase mapping, Phys. Procedia 69 (2015) 227–236.
[22] M.G. Makowska, et al., In situ time-of-flight neutron imaging of NiO–YSZ anode support reduction under influence of stress, J. Appl. Crystallogr. 49 (2016) 1674–1681.
[23] M. Morgano, et al., Investigation of the effect of laser shock peening in additively manufactured samples through Bragg edge neutron imaging, Addit. Manuf. (2020), 101201.
[24] T. Shinohara, et al., The energy-resolved neutron imaging system, RADEN, Rev. Sci. Instrum. 91 (2020), 043302.
[25] A. Tremsin, J. Vallerga, Unique capabilities and applications of microchannel plate (MCP) detectors with Medipix/Timepix readout, Radiat. Meas. 130 (2020), 106228.
[26] A. Tremsin, J. Vallerga, J. McPhate, O. Siegmund, Optimization of Timepix count rate capabilities for the applications with a periodic input signal, J. Instrum. 9 (2014) C05026.
[27] M. Boin, NXS: a program library for neutron cross section calculations, J. Appl. Crystallogr. 45 (2012) 603–607.
[28] A. Leicht, M. Rashidi, U. Klement, E. Hryha, Effect of process parameters on the microstructure, tensile strength and productivity of 316L parts produced by laser powder bed fusion, Mater. Charact. 159 (2020), 110016.
[29] A. Leicht, C. Yu, V. Luzin, U. Klement, E. Hryha, Effect of scan rotation on the microstructure development and mechanical properties of 316Lva parts produced by laser powder bed fusion, Mater. Charact. (2020), 110309.
[30] S. Van Petegem, et al., In-situ neutron diffraction during biaxial deformation, Acta Mater. 105 (2016) 404–416.
[31] J. Oliveira, et al., Gas tungsten arc welding of as-rolled crmnfeconi high entropy alloy, Mater. Des. 189 (2020), 108505.
[32] G. Schajer, E. Altus, Stress calculation error analysis for incremental hole-drilling residual stress measurements, J. Eng. Mater. Technol. 118 (1996) 120–126.
[33] N. Kalentics, et al., 3D laser shock peening–a new method for the 3D control of residual stresses in selective laser melting, Mater. Des. 130 (2017) 350–356.
[34] A.S. Wu, D.W. Brown, M. Kumar, G.F. Gallegos, W.E. King, An experimental investigation into additive manufacturing-induced residual stresses in 316L stainless steel, Metall. Mater. Trans. A 45 (2014) 6260–6270.
[35] D. Brown, et al., Neutron diffraction measurements of residual stress in additively manufactured stainless steel, Mater. Sci. Eng. A 678 (2016) 291–298.
[36] N. Kalentics, et al., Tailoring residual stress profile of selective laser melted parts by laser shock peening, Addit. Manuf. 16 (2017) 90–97.
[37] S. Goel, et al., Residual stress determination by neutron diffraction in powder bed fusion-built alloy 718: influence of process parameters and post-treatment, Mater. Des. 195 (2020), 109045.
[38] Y. Wang, J. Shi, Y. Liu, Competitive grain growth and dendrite morphology evolution in selective laser melting of Inconel 718 superalloy, J. Cryst. Growth 521 (2019) 15–29.
[39] A. Staub, A.B. Spierings, K. Wegener, Correlation of meltpool characteristics and residual stresses at high laser intensity for metal lpbf process, Adv. Mater. Process. Technol. 5 (2019) 153–161.
[40] H. Ali, H. Ghadbeigi, K. Mumtaz, Effect of scanning strategies on residual stress and mechanical properties of selective laser melted Ti6Al4V, Mater. Sci. Eng. A 712 (2018) 175–187.